A mechanistic model for breakage in population balances of granulation: Theoretical kernel development and experimental validation

Rohit Ramachandran[a], Charles D. Immanuel[a,*], Frantisek Stepanek[a], James D. Litster[b], Francis J. Doyle III[c]

[a] Centre for Process Systems Engineering, Department of Chemical Engineering, Imperial College London, London SW7 2AZ, UK
[b] School of Chemical Engineering, Purdue University, West Lafayette, IN 47907-2100, USA
[c] Department of Chemical Engineering, University of California at Santa Barbara, Santa Barbara, CA 93106, USA

ABSTRACT

In this study, a dynamic model is presented for the granulation process, employing a three-dimensional population balance framework. The major focus of this work is the theoretical development and experimental validation of a novel mechanistic breakage kernel that is incorporated within the population balance equation. Qualitative validation of breakage kernel/model was first performed and trends of lumped properties (i.e., total particles, average size, binder content and porosity) and distributed properties (i.e., granule size and fractional binder content) show good agreement with the expected phenomenological behaviour. Successful high-shear mixer granulation experiments using glass-ballotini as the primary powder and poly-vinyl alcohol in water (PVOH-H_2O) as the liquid binder were then carried out to mimic predominantly breakage-only behaviour whereby the rate of breakage was greater than the rates of nucleation and aggregation. Good agreement between experimental and simulation results were obtained for the granule size distribution under different operating conditions. In addition, accurate model predictions were obtained for the evolution of the lumped properties.

© 2008 Published by Elsevier B.V. on behalf of The Institution of Chemical Engineers.

Keywords: Granulation; High-shear mixing; Multi-dimensional population balance; Breakage; Mechanistic kernels; Experimental validation

1. Introduction

Granulation is a particle production process of converting fine powdery solids into larger free-flowing agglomerates. It finds application in a wide range of industries (e.g. pharmaceuticals, fertilisers and minerals). Granulated products often have notable improvements compared to their ungranulated form and some of these include increased bulk density, improved flow properties and uniformity in the distribution of multiple solid components. Granulation processes have been ubiquitous in the industry for many years with significant research undertaken to gain further insight into the underlying phenomena occurring during the process. However, industrial granulation processes are by-and-large operated in a highly inefficient manner with large recycle ratios within the process

(3–4:1, recycle/product) (Mort, 2005). Therefore, an integrated systems modelling approach will be a crucial aid to mitigate this situation (Mort, 2005; Bardin et al., 2004; Knight et al., 1998; Litster, 2003). Furthermore, a comprehensive model of the process will enable an analysis of the system dynamics and the formulation of a suitable control strategy, which potentially could contribute to a more efficient operation of the process (Mort, 2005; Bardin et al., 2004; Knight et al., 1998; Litster, 2003).

In granulation, it is now generally accepted that three rate processes are sufficient to elucidate its behaviour. These are namely wetting and nucleation; consolidation and growth; and breakage and attrition (Litster and Ennis, 2004). The formation of granules is first initiated by the nucleation of fine powder (primary particles). This involves the distribution of liquid binder among the powder, followed by the penetration

of the droplet into the powder wherein the binder droplet will capture the particles surrounding it thereby converting it into a nucleus. The nuclei particles will continue to grow via aggregation and consolidation, as they collide with other (nuclei) particles and the walls of the granulator. Granule breakage may also result due to collisions. Previously, a methodology for the aggregation and nucleation mechanistic kernels has been developed and validated (Immanuel and Doyle, 2005; Poon et al., 2008, in press).

In the recent years, significant research on the understanding of granulation has been carried out. This has resulted in many research advances with regard to accurate modelling of the granule mechanisms, especially in the case of aggregation. Breakage on the other hand, like nucleation is less understood compared to aggregation (Liu et al., 2008). However, understanding breakage behaviour is of importance as breakage of wet granules will influence and control the final granule size distribution, especially in high-shear granulators (Iveson et al., 2001; Liu et al., 2008). Breakage can also be used to limit maximum granule size or help distribute a viscous binder, which would lead to an increase in the aggregation efficiency. Many of the existing breakage models/kernels are empirical and do not explicitly account for the dependence of material properties and process/design parameters. In other cases, studies have neglected breakage altogether, lumping the breakage mechanism in their aggregation model. Given the importance of breakage and the lack of suitable breakage models, this study is concerned with the qualitative and quantitative development and validation of a novel multi-dimensional mechanistic breakage model that can explicitly account for the dependence of key material properties and process/design parameters on important granule properties. A detailed sensitivity analysis will also be undertaken to quantify effects of key properties/parameters on granule properties.

2. Background

The granulation breakage process is described by a three-dimensional population balance model, which accounts for granule size, binder content and porosity. The potential heterogeneity of the population distribution with respect to all three attributes is such that lumping in any of these dimensions would result in considerable model errors (Iveson, 2002). In formulating the three-dimensional population balance, the three particle attributes are recast in terms of their individual volumes of solid (s), liquid (l) and gas (g) (Verkoeijen et al., 2002). The purpose of modelling the granulation process in terms of its individual volumes enables decoupling of the individual meso-scopic processes (i.e., aggregation, consolidation, etc.). This essentially offers two advantages. Firstly, one could model a single rate process at a time. Secondly, the mutually exclusive character of the internal coordinates substantially improves the solution of the model as rate processes with differing time constants are segregated. The resulting three-dimensional population balance equation is then given by

$$\frac{\partial}{\partial t}F(s,l,g,t) + \frac{\partial}{\partial g}\left(F(s,l,g,t)\frac{dg}{dt}\right) + \frac{\partial}{\partial s}\left(F(s,l,g,t)\frac{ds}{dt}\right)$$
$$+ \frac{\partial}{\partial l}\left(F(s,l,g,t)\frac{dl}{dt}\right) = \Re_{break} \tag{1}$$

where $F(s,l,g,t)$ represents the population density function such that $F(s,l,g,t)\,ds\,dl\,dg$ is the moles of granules (adopt-

ing a number-based population balance instead of mass or volume-based) with solid volume between s and $s + ds$, liquid volume between l and $l + dl$ and gas volume between g and $g + dg$. The partial derivative term with respect to s, accounts for the layering of fines onto the granule surfaces; the partial derivative term with respect to l accounts for the drying of the binder and the re-wetting of granules; the partial derivative with respect to g accounts for consolidation which due to compaction of the granules, results in an increase of pore saturation and decrease in porosity. In this study, layering and drying are neglected. The breakage term ($\Re_{break}$) is mathematically described in two parts; the breakage kernel (k_{eff}) and the breakage function (b). The former describes the rate at which a particle of size s, l and g breaks into a fragments of size s_1, l_1 and g_1. The latter describes the sizes of these fragments formed. Therefore, $\Re_{break}$ is defined in Eqs. (2) and (3):

$$\Re_{break}^{formation} = \int_s^\infty \int_l^\infty \int_g^\infty k_{break}(s_1,l_1,g_1)b(s,l,g,s_1,l_1,g_1)$$
$$\times F(s_1,l_1,g_1,t)\,ds_1\,dl_1\,dg_1 \tag{2}$$

$$\Re_{break}^{depletion} = k_{break}(s,l,g)F(s,l,g,t) \tag{3}$$

The consolidation model is represented by an empirical exponential decay relation and is shown in Eq. (5). The porosity of granules is defined by Eq. (4) and substituting Eq. (4) into Eq. (5) gives a formal expression explicitly in terms of the three independent internal coordinates, which can then be used in Eq. (1):

$$\varepsilon = \frac{l+g}{s+l+g} \tag{4}$$

$$\frac{d\varepsilon}{dt} = -c(\varepsilon - \varepsilon_{min}) \tag{5}$$

$$\frac{dg}{dt} = -c\frac{s+l+g}{s(1-\varepsilon_{min})}\left[l - \frac{\varepsilon_{min}s}{1-\varepsilon_{min}} + g\right] \tag{6}$$

Here ε_{min} is the minimum porosity of the granules and c is the compaction rate constant.

2.1. Breakage kernel

A primary challenge in the development of the population balance models, is the identification of appropriate kernels (rate constants) that describe the individual mechanisms. While the development of a multi-dimensional population balance model is motivated by the physics of the problem, it is a tougher task to obtain three-dimensional kernels that account for the dependence of the rates on the particle traits (i.e., size, binder content and porosity). Compared to the aggregation kernel, research on breakage kernels is still in its infancy. Sanders et al. (2003) and Biggs et al. (2003) attempted to model breakage as a negative aggregation rate process, essentially reporting a reduced aggregation rate constant. However, there are problems with this approach as aggregation is a second order rate process and breakage is a first order rate process. Therefore, trying to incorporate breakage in an aggregation kernel is fundamentally flawed and will not succeed with any physical basis (Reynolds et al., 2005). In other studies, complexity of breakage models extend from empirical models based on experimental observations of breakage (Van den Dries et al., 2003; Salman et al., 2003), to binary breakage

functions (Tan et al., 2004, 2005) that describe how a granule breaks into large and small fragments. These models however, do not explicitly account for any process or material properties to determine breakage rates. More recently, Dhanarajan and Bandyopadhyay (2007) presented an energy-based model for high-shear granulation processes, whereby the extent of granule breakage was considered to be directly proportional to the impact-energy and inversely proportional to granule strength. While their model showed a close correspondence between the simulated and experimental results for a particular granulation recipe, it lacked a rigorous physical basis in the following ways. Firstly, it assumed that kinetic energy was a function of only mass (neglecting velocity) and that all collisions were elastic (neglecting loss of kinetic energy due to inelasticity). Secondly, it assumed that granule strength was primarily a function of binder content, without considering the effect of binder properties such as viscosity, surface tension and contact-angle. To date, there is no comprehensive breakage kernel in the literature that has sound physical basis and does not make any simplifying assumptions.

2.2. Deriving the breakage function

As seen from Eqs. (2) and (3), breakage is described by the breakage function (b) and the breakage kernel (K_{break}). The breakage function describes how fragments, resulting from the breakup of granules, are distributed in terms of their volume. There are several possible functional forms for this distribution, given either by continuous (e.g. normal or log-normal distribution) or discrete (e.g. binary) distributions. The breakage function used in this study is based on the work of Pinto et al. (2007), Pinto (2008), Pinto et al. (2008). Based on the probabilities of particles in a particular finite volume breaking to form daughter particles in one or more smaller finite volumes in the three-dimensional space, they performed a numerical operation that was able to describe the distribution of these fragments. Using these probabilities, semi-analytical solutions were derived for the triple integrals present in $\Re_{break}^{formation}$ (see Eq. (2)), thus eliminating the integrals altogether and aiding the numerical solution. In the next section, the development of the breakage kernel is described.

3. Mechanistic kernel development

A granule will break if the external stress during an impact exceeds the intrinsic strength of the granule. This is analogous to the Stokes' deformation number criteria for breakage whereby a granule will break if the applied kinetic energy during an impact is greater than the energy required for breakage (Iveson et al., 2001). Therefore the proposed kernel form is defined in Eqs. (7) and (8):

$$K_{break}(s, l, g) \propto \frac{\text{external stress}}{\text{intrinsic strength}} \tag{7}$$

$$K_{break}(s, l, g) = A \times \frac{\text{external stress}}{\text{intrinsic strength}} \tag{8}$$

where K_{break} is the breakage kernel, A is a proportionality constant and s, l, g are the respective volumes of solid, liquid and gas pertaining to individual finite volumes (bins). Units are dimensionless. If K_{break} is less than one, $K_{break} = 0$, as the external stress applied is less than the intrinsic strength of the granule and the granule does not break.

3.1. External stress

To calculate the external stress (σ_{ext}), external forces (F_{ext}) acting on a granule and their area of contact (A_c) need to be evaluated. External stress (N m^{-2}) is then defined in Eq. (9):

$$\sigma_{ext}(s, l, g) = \frac{F_{ext}(s, l, g)}{A_c(s, l, g)} \tag{9}$$

3.1.1. Forces
The external forces on the granules/particles can occur via the following ways:

- **Case 1:** Forces due to fluid flow.
- **Case 2:** Forces due to particle–particle collisions.
- **Case 3:** Forces due to particle–wall collisions.
- **Case 4:** Forces due to particle–impeller collisions.

3.1.1.1. Case 1: forces due to fluid flow. The force (F_{flu}) on a particle in laminar flow is defined in Eq. (10):

$$F_{flu}(s, l, g) = 6\pi\mu r v \tag{10}$$

where r is the radius of the particle, v is the velocity of the particle relative to the fluid and μ is the viscosity of the fluid. The force (F_f) on a particle in turbulent flow is defined in Eq. (11):

$$\begin{aligned} F_f(s, l, g) &= \frac{1}{2}\rho C_d A v^2 \\ &= \frac{1}{2}\pi\rho C_d r^2 v^2 \end{aligned} \tag{11}$$

where ρ is the density of the fluid and C_d is the *drag coefficient* which for a spherical particle is 0.47. C_d increases as non-sphericity increases. Reynold's number (Re) which is defined in Eq. (12) is calculated to determine if conditions are either laminar or turbulent. L is the characteristic length.

$$Re = \frac{\rho v L}{\mu} \tag{12}$$

3.1.1.2. Case 2: forces due to particle–particle collisions. In the case of particle–particle collisions, a particle with mass m_a and initial velocity u_a collides head-on with another particle of mass m_b and initial velocity u_b. Based on the conservation of momentum, momentum before impact ≡ momentum after impact. Assuming that the total energy input into the system is constant, $u_{a,b}$ (initial velocities of either particle) can be defined in Eq. (13) as

$$u_{a,b}(s, l, g) = \left(\frac{1}{m_{a,b}(s, l, g)}\right)^{0.5} \tag{13}$$

where m is the mass of either particle. Therefore,

$$m_a(s, l, g)(v_a(s, l, g) - u_a(s, l, g))$$
$$= m_b(s, l, g)(v_b(s, l, g) - u_b(s, l, g)) \tag{14}$$

where v_a and v_b are the final velocities of particles a and b respectively, which are yet to be determined. Given,

$$e(s, l, g) = \frac{v_b(s, l, g) - v_a(s, l, g)}{u_a(s, l, g) - u_b(s, l, g)} \tag{15}$$

where e is the coefficient of restitution whereby $e = 1$ denotes perfectly elastic collisions and $e = 0$ denotes perfectly inelastic collisions. e is material specific and is known a priori. Solving Eqs. (14) and (15), v_a and v_b are obtained.

Once v_a and v_b are obtained, there are many approaches to modelling the collision interactions between particles. In this work, a harmonic spring model that is realistically able to model collisions between particles is used (Luding et al., 1994). Two particles interact when their relative distance $r_{ab} = |\mathbf{r}_{ab}|$ (where r_{ab} points from the centre of a to the center of b) is smaller than the sum of their radii (the radius of the particles R_a and R_b). In this regime, $R_a + R_b > r_{ab}$, an elastic restoration force (F_{el}) can be defined as seen in Eq. (16).

$$F_{el}(s_a, l_a, g_a, s_b, l_b, g_b) = -k[(R_a + R_b) - r_{ab}]\mathbf{n}_{ab} \tag{16}$$

where $\mathbf{n}_{ab} = \mathbf{r}_{ab}/r_{ab}$ is the normal direction of contact and k is a force constant. $s_a, l_a, g_a, s_b, l_b, g_b$ are the component volumes of particles a and b respectively. Secondly, a frictional force in the normal direction is defined as seen in Eq. (17):

$$F_{\text{fric}}(s_a, l_a, g_a, s_b, l_b, g_b) = -\gamma_N \tilde{m}[\mathbf{v}_{ab} \cdot \mathbf{n}_{ab}]\mathbf{n}_{ab} \tag{17}$$

where $\mathbf{v}_{a,b}$ is the relative velocities of particles a and b, $\tilde{m}$ is twice the reduced mass of particles a and b (i.e., $2m_a m_b/(m_a + m_b)$), $d = R_a + R_b$, γ_N is the damping coefficient. $\mathbf{r}_{a,b}$ is then defined in Eq. (18), where $x_{\max}$ is the maximum depth of penetration and considering nonlinear interactions between particles, is defined in Eq. (19)(Luding et al., 1994). Based on the Hertz interaction law, $\beta = 0.5$ (Luding et al., 1994). $\bar{E} = (E/[3(1 - \sigma^2)])$, where E is the Young's modulus and σ is the Poisson ratio. d is the sum of the radii R_a and R_b. Both E and σ are material specific and are known a priori:

$$\mathbf{r}_{ab} = R_a + R_b - x_{\max} \tag{18}$$

$$x_{\max} = \left[1 + \frac{\beta}{2}\right]^{1/2+\beta} \left[\frac{m_a}{\bar{E}d^{1-\beta}}\right]^{1/2+\beta} (u_a)^{2/2+\beta} \tag{19}$$

Similarly, the collision time (t_c) is defined in Eq. (20):

$$t_c = I(\beta)\frac{x_{\max}}{u_a} \tag{20}$$

where $I(\beta) = 2.94$ (Luding et al., 1994). Subsequently, k and γ_N are obtained as follows:

$$k = \frac{m_a}{2}\left(\frac{\pi}{t_c}\right)^2 \tag{21}$$

$$\gamma_N = \frac{-2\ln e}{t_c} \tag{22}$$

The total external force as a result of particle–particle collisions is then obtained as seen in Eq. (23).

$$F_{\text{ext}}(s_a, l_a, g_a, s_b, l_b, g_b)$$
$$= F_{el}(s_a, l_a, g_a, s_b, l_b, g_b) + F_{\text{fric}}(s_a, l_a, g_a, s_b, l_b, g_b) \tag{23}$$

3.1.1.3. Case 3: forces due to particle–wall collisions. In the case of particle–wall collisions, a particle a collides with the wall (interior surfaces) of the granulator (denoted with subscript b). Forces are derived as in case 2 with a few minor simplifi-

cations. As a result of the wall being a flat plane, $d \rightarrow (d/2)$, $\tilde{m} \rightarrow m_a$, $\mathbf{r}_{ab} \rightarrow \mathbf{r}_a$. As a result of the wall being stationary ($u_b = 0$) and $m_b \gg m_a$, the conservation of momentum equation can also be simplified such that final velocity of particle a can be calculated as $v_a = -e \times u_a$. Total external force is then defined as

$$F^{\text{ext}}(s_a, l_a, g_a) = F^{el}(s_a, l_a, g_a) + F^{\text{fric}}(s_a, l_a, g_a) \tag{24}$$

3.1.1.4. Case 4: forces due to particle–impeller collisions. In the case of particle–wall collisions, a particle a collides with the impeller surfaces (denoted with subscript b). Forces are derived as in case 3 with a minor modification. Unlike particle–wall collisions, although $m_b \gg m_a$, $u_b \neq 0$. As a result, the conservation of momentum equation can now be simplified such that $v_a = e \times 2u_b$. Total external force is then defined as

$$F^{\text{ext}}(s_a, l_a, g_a) = F^{el}(s_a, l_a, g_a) + F^{\text{fric}}(s_a, l_a, g_a) \tag{25}$$

For all cases of particle–particle/wall/impeller collisions, 1-dimensional head-on collisions are considered so as to effect the maximum force experienced by the particle(s). The kernel can also be adapted to take into account two-dimensional collisions (i.e., particles colliding at an angle) and/or one-dimensional collisions of a faster moving particle hitting a slower moving particle as they move in the same direction.

3.1.2. Contact area
The contact area in which the different forces act upon are derived for the three cases.

3.1.2.1. Case 1: contact area for forces due to fluid flow. The force acts on the entire particle surface. Therefore contact area (A_c) is defined in Eq. (26) as

$$A_c(s_a, l_a, g_a) = 4\pi R_a^2(s_a, l_a, g_a) \tag{26}$$

3.1.2.2. Case 2: contact area for forces due to particle–particle collisions. In the case of particle–particle collisions, the contact area upon impact is circular in shape (Stachowiak and Batchelor, 2005). A reduced Young's modulus (E') is first defined in Eq. (27) as

$$E'(s_a, l_a, g_a) = \left(\frac{1}{2}\left[\frac{1 - \sigma_a^2}{E_a} + \frac{1 - \sigma_b^2}{E_b}\right]\right)^{-1} \tag{27}$$

where σ_a and σ_b are the Poisson ratios of particles a and b; and E_a and E_b are the Young's moduli for particles a and b. A reduced radius (R') is then defined in Eq. (28):

$$R'(s_a, l_a, g_a) = \left[2\left(\frac{1}{R_A} + \frac{1}{R_B}\right)\right]^{-1} \tag{28}$$

where R_a and R_b are the radii of particles a and b respectively. Contact radius (r_c) and contact area (A_c) are then defined respectively in Eqs. (29) and (30) as

$$r_c(s_a, l_a, g_a) = \frac{3F_{\text{ext}}(s_a, l_a, g_a)R'}{E'} \tag{29}$$

$$A_c(s_a, l_a, g_a) = \pi r_c^2(s_a, l_a, g_a) \tag{30}$$

3.1.2.3. Cases 3 and 4: contact area for forces due to particle–wall/impeller collisions. In the case of particle–wall

collisions and particle–impeller collisions, the contact area upon impact is elliptical in shape (Stachowiak and Batchelor, 2005). A reduced radius (R') is defined in Eq. (31) as follows:

$$R' = \left[\frac{1}{R_{Ax}} + \frac{1}{R_{Ay}} \right]^{-1} \tag{31}$$

where R_{Ax} and R_{Ay} are the radii of particle a in the x and y directions. R_{Bx} and $R_{By} = \infty$ since one plane (wall or impeller) has an infinite radius of curvature in both directions. The reduced Young's modulus E' is defined as in case 2. Contact area A_c is then defined in Eq. (32):

$$A_c(s_a, l_a, g_a) = \pi AB \tag{32}$$

where A and B are the radii of the eclipse in the x and y directions. A and B are defined in Eqs. (33) and (34):

$$A = \left[\frac{6\bar{k}^2 \bar{\varepsilon} FR'}{\pi E'} \right]^{1/3} \tag{33}$$

$$B = \left[\frac{6\bar{\varepsilon} FR'}{\pi \bar{k} E^1} \right]^{1/3} \tag{34}$$

where $\bar{\varepsilon} = 1.0003 + (0.5968 R_x/R_y)$ and $\bar{k} = 1.0339(R_x/R_y)^{0.636}$. $R_x/R_y = 1$ for spherical particles. $\bar{\varepsilon}$ is a simplified integral and $\bar{k}$ is an ellipticity parameter.

3.2. Intrinsic strength

The different types of bonds that may exist within the types of granules are classified as follows: (1) forces due to immobile films, (2) forces due to mobile liquid bridges, (3) forces due to solid bridges, (4) forces due to attractive effects between solid particles and (5) forces due to mechanical interlocking between solid particles. The relative importance of these bonding forces varies from case to case, depending on the type and size of the granule. In the case of wet granules, contributions by (1), (3), (4) and (5) are usually negligible and the strength of wet granules are primarily determined by liquid bridge forces (Reynolds et al., 2005). The liquid bridge is therefore responsible for holding two or more particles together (Simons, 2007; Willett et al., 2007; Simons et al., 1994; Iveson, 2002)(see Fig. 1).
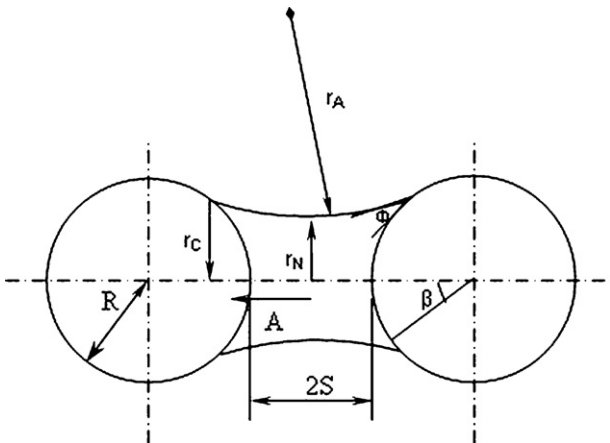

Fig. 1 – Schematic of a liquid bridge between two equi-sized particles.

In the current breakage model, any granule from a particular finite volume can break into m daughter particles of volume fraction θ_a such that $\sum_{a=1}^{m} \theta_a = 1$. As a first attempt to derive the breakage kernel, $m = 2$ and $\theta_1 = \theta_2 = 0.5$. Therefore, this means that any granule from any finite volume comprises of two smaller equi-sized particles held together by one liquid bridge. The following theoretical development of the kernel in this study is based on the above qualification. However, the theory can be extended to handle multiple fragments ($m > 2$) which would result in multiple liquid bridges and possibly unequal-sized fragments (Ramachandran, 2008).

The liquid bridge forces (F_{int}) are in turn made up of capillary forces (F_{cap}), viscous forces (F_{vis}) and frictional forces (F_f). Viscous forces are an important factor to account for, as liquid bridges cannot be regarded as stationary and the inter-particle attractive force depends on the viscosity of the binder liquid. The effects of buoyancy forces are negligible (Princen, 1968) and as a result are not accounted for. Similarly the effects of gravity are negligible, and therefore neglected (Willett et al., 2007). F_{cap} consists of two components, the force due to surface tension (F_γ) and the force due to reduced hydrostatic pressure (F_p). The capillary suction pressure (ΔP_{cap}) across the liquid–vapour interface is given by the Laplace–Young equation (Simons, 2007; Willett et al., 2007) and is defined in Eq. (35):

$$\Delta P_{cap}(s_a, l_a, g_a) = \frac{2\gamma_{LV}}{r} = \gamma_{LV} \left(\frac{1}{r_A} + \frac{1}{r_N} \right)$$
$$= \gamma_{LV} \left(\frac{\ddot{y}}{[1 + \dot{y}^2]^{3/2}} + \frac{1}{y(1 + \dot{y}^2)^{1/2}} \right) \tag{35}$$

where γ_{LV} is the liquid surface tension, r is the curvature of the bridge surface which can be calculated from the two principal radii of curvature of the surface, r_A and r_N as shown in Fig. 1. $\dot{y}$ and $\ddot{y}$ are the first and second derivatives of the liquid bridge profile. Eq. (35) cannot be solved analytically and either the boundary or gorge methods have to be used to solve them numerically (Hotta et al., 1974; Lian et al., 1993). The latter method gave a better estimate of the total force (Lian et al., 1993) and therefore is used in this work. F_γ, F_p and F_{cap} are then defined in Eqs. (36)–(38):

$$F_\gamma(s_a, l_a, g_a) = 2\pi r_A \gamma_{LV} \tag{36}$$

$$F_p(s_a, l_a, g_a) = -\pi r_A^2 \Delta P_{cap}$$
$$= -\pi r_1^2 \gamma_{LV} \left[\frac{1}{r_A} + \frac{1}{r_N} \right] \tag{37}$$

$$F_{cap}(s_a, l_a, g_a) = F_\gamma + F_p = 2\pi r_A \gamma_{LV} - \pi r_A^2 \gamma_{LV} \left[\frac{1}{r_A} + \frac{1}{r_N} \right] \tag{38}$$

r_A and r_N are defined in Eqs. (39) and (40),

$$r_A(s_a, l_a, g_a) - r_N(s_a, l_a, g_a) = \frac{A}{\tan((\pi/2) - \beta - \phi)} + R \sin\beta \tag{39}$$

$$r_N(s_a, l_a, g_a) = (-1)^n \{ A^2 + [R \sin\beta - (r_A - r_N)]^2 \}^{1/2} \tag{40}$$

where ϕ is the contact angle, β is the half-filled angle and R is the reduced radius defined in Eq. (28). n and A are defined in Eqs. (41) and (42) respectively

$$n = \left[0, \left((\beta + \phi) > \frac{\pi}{2} \right) \text{ or } 1, \left((\beta + \phi) \leq \frac{\pi}{2} \right) \right] \tag{41}$$

$$A(s_a, l_a, g_a) = S + R(1 - \cos\beta) \tag{42}$$

where S is half of the separation distance (see Fig. 1) and is defined in Eq. (43) as

$$S(s_a, l_a, g_a) = \left[1 + \frac{\pi}{2}\right] \times V_{br}^{1/3} \tag{43}$$

The liquid bridge volume (V_{br}) is known a priori and is determined by the amount of liquid on the surface (surfaces of the two smaller particles that comprise of the larger granule) that can be used to form the liquid bridge. If the volume of air (in both smaller particles) is greater than the volume of liquid (in both smaller particles) for a particular finite volume, no liquid is available to form liquid bridges. Available liquid is defined as the difference between volumes of liquid and air. V_{br} is then defined in Eq. (44) as

$$\begin{aligned}
V_{br}(s_a, l_a, g_a) &= 2\pi\left[A(r_A - r_N)^2 + r_A^3\left(\frac{A}{r_A} - \frac{A^3}{3r_A^3}\right)\right.\\
&\quad + r_A^2(r_A - r_A)\sin^{-1}\left(\frac{A}{r_A}\right)\\
&\quad + (-1)^n A(r_A - r_N)(r_A^2 - A^2)^{1/2}\\
&\quad \left. - R(A - S)^2 - \frac{(A - S)^3}{3}\right]
\end{aligned} \tag{44}$$

Knowing V_{br}, and substituting Eqs. (42), (43), (40), (39) in Eq. (44), β can be solved for iteratively for each bin. Thereafter, Eqs. (39) and (40) can be solved for r_A and r_N.

The contact radius r_c, is defined in Eq. (45) as

$$r_c(s_a, l_a, g_a) = R\sin\beta \tag{45}$$

The viscous force F_{vis}, is defined in Eq. (46) as

$$F_{vis}(s_a, l_a, g_a) = \frac{3}{2}\pi\mu R^2 \frac{1}{S}\frac{da}{dt} \tag{46}$$

where μ is the liquid viscosity and da/dt is the half-gap velocity which without exact knowledge, is a potential tuning parameter. The frictional force, which is due to the work of adhesion on liquid and the corresponding inter-particle contact area is defined in Eq. (47) as

$$F_f(s_a, l_a, g_a) = \gamma_{LV}(\cos\theta + 1)\frac{\pi r_c^2 \times (1/circ)}{S} \tag{47}$$

where $circ$ is the circularity index of the particle. For a sphere, $circ = 1$ and $circ \to 0$ as the non-sphericity increases. The total force of the liquid bridge is then defined in Eq. (48):

$$F_{int}(s_a, l_a, g_a) = F_{cap} + F_{vis} + F_f \tag{48}$$

The intrinsic strength due to the liquid bridge is then defined in Eq. (49) as

$$\sigma_{liq}(s_a, l_a, g_a) = \frac{F_{int}}{2\pi r_c^2} \tag{49}$$

When an external force is applied to the particles, there exist solid–solid attractions (known as cohesive strength) which need to be overcome. This is defined in Eq. (50) as

$$\sigma_c(s_a, l_a, g_a) = \frac{2\gamma_s 4\pi R^2}{V_{part}} \tag{50}$$

where γ_s is the surface energy of the solid and V_{part} is the volume of the particle. Therefore, the intrinsic strength is now defined in Eq. (51) as

$$\sigma_{int}(s_a, l_a, g_a) = \sigma_{liq} + \sigma_c \tag{51}$$

3.3.   Overall kernel formulation

In the above section, σ_{ext} and σ_{int} were derived based on first principles allowing for the formulation of the overall breakage kernel. For cases 1, 3 and 4, K_{break} is defined in Eq. (52):

$$K_{break}(s_a, l_a, g_a) = \frac{\sigma_{ext}(s_a, l_a, g_a)}{\sigma_{int}(s_a, l_a, g_a)} \tag{52}$$

For case 2, K_{break} is defined in Eq. (53).

$$K_{break}(s_a, l_a, g_a, s_b, l_b, g_b) = \frac{\sigma_{ext}(s_a, l_a, g_a, s_b, l_b, g_b)}{\sigma_{int}(s_a, l_a, g_a)} \tag{53}$$

Although the external forces for each of the cases have been derived separately for the different cases, the actual external forces applied on the particle are based on the probability of a particle of characteristic (s_a, l_a, g_a) hitting either a particle of characteristic (s_b, l_b, g_b), a wall surface, or the impeller surface. Fluid forces act in addition to these particle–particle, particle–wall and particle–impeller forces. The system is assumed to be free in-space such that each particle is able to collide with another particle, a wall or the impeller. A probability (in terms of the surface area) is assigned for each type of collision that may occur. Therefore the three-dimensional kernels derived for cases 1, 3 and 4 and the six-dimensional kernel derived for case 2 are transformed into an effective 3-dimensional kernel (K_{break}^{eff}) as defined in Eq. (54) as

$$\begin{aligned}
&K_{break}^{eff}(s_a, l_a, g_a)\\
&= \Sigma_{s_b=1}^{s_{upper}} \Sigma_{l_b=1}^{l_{upper}} \Sigma_{g_b=1}^{g_{upper}} \left[\frac{\sigma_{ext}^{particle}(s_a, l_a, g_a, s_b, l_b, g_b)}{\sigma_{int}(s_a, l_a, g_a)}\right.\\
&\quad \left. \times F(s_b, l_b, g_b) \times N_a \times \frac{SA(s_b, l_b, g_b)}{SA + WA + IA}\right]\\
&\quad + \left[\frac{\sigma_{ext}^{wall}(s_a, l_a, g_a)}{\sigma_{int}(s_a, l_a, g_a)} \times \frac{WA}{SA + WA + IA}\right]\\
&\quad + \left[\frac{\sigma_{ext}^{impeller}(s_a, l_a, g_a)}{\sigma_{int}(s_a, l_a, g_a)} \times \frac{IA}{SA + WA + IA}\right]\\
&\quad + \left[\frac{\sigma_{ext}^{fluid}(s_a, l_a, g_a)}{\sigma_{int}(s_a, l_a, g_a)}\right]
\end{aligned} \tag{54}$$

where F is the particle density, WA is the total wall surface area, kg is the total surface area of all the particles, SA is the surface area of an individual particle, IA is the impeller surface area and N_a is Avagardo's constant, s_{upper}, l_{upper} and g_{upper} are the upper limits of the finite volumes in each of the three solid, liquid and gas dimensions. $K_{eff}^{break}(s_a, l_a, g_a)$ is updated at each time step as $F(s_a, l_a, g_a)$ changes at each time step. In the next section, simulation results of the breakage model are presented. The mechanistic kernel is qualitatively compared with an existing empirical and semi-empirical kernel from the literature. Thereafter, effects of material properties and process/design parameters on granule characteristics are examined.

| Table 1 – Nominal values of material properties and process/design parameters.		
Property/parameter	Value	Unit
γ_s	4.48×10^{-2}	$N\,m^{-2}$
η	7.28×10^{-2}	$N\,m^{-2}$
μ_l	1.0×10^{-3}	Pa s
ϕ	7.54×10^{-1}	rad
ρ_s	2.72×10^3	$kg\,m^{-3}$
ρ_l	1.0×10^3	$kg\,m^{-3}$
μ_a	1.85×10^{-5}	Pa s
E_p	4.50×10^{10}	Pa
E_w	7.0×10^{10}	Pa
E_i	2.0×10^{11}	Pa
σ_p	0.22	–
σ_w	0.17	–
σ_i	0.30	–
e_p	0.60	–
e_w	0.50	–
e_i	0.80	–
circ	1.0	–
C_d	0.47	–
θ	0.50	–
TSA	2.02×10^{-1}	m^2
WA	6.13×10^{-1}	m^2
IA	3.06×10^{-1}	m^2
D_{lower}	246	μm
A	1.5×10^{-8}	s^{-1}
$\frac{da}{dt}$	5.0×10^{-2}	$m\,s^{-1}$

TSA refers to the total surface area of the initial seed particles. TSA will change as the particle density changes during the course of granulation.

Fig. 2 – Shape of the mechanistic kernel (Eq. (54)) with respect to two dimensions keeping the third constant: (a) volume of gas constant, (b) volume of liquid constant and (c) volume of solid constant.

4. Simulation results of the breakage model

All model simulations were carried out on a 2 GHz Intel dual-core single processor desktop computer with 1 GB RAM, using the Intel Fortran compiler. Simulation time was 1800 s. Table 1 presents the nominal values of all material properties and process/design parameters used in the simulations. The values correspond to a hypothetical case of limestone as the primary powder, water as the liquid binder, steel blades as the impeller, and glass walls as the interior surfaces. High-shear laboratory-scale dimensions are assumed for the granulator geometry. Any viscosities and surface tensions reported are obtained for conditions at room temperature and pressure (r.t.p.).

4.1. Comparison of the mechanistic kernel with empirical and semi-empirical kernels

Fig. 2 a–c depicts the simulated shape of the mechanistic breakage kernel (Eq. (54)) with respect to two dimensions (i.e., solid–liquid, solid–gas or liquid–gas) keeping the third dimension constant (i.e., solid, liquid or gas). The shapes observed are in agreement with expected phenomenological behaviour. In Fig. 2 a, for a very small liquid content and constant gas volume, it can be observed that K_{break}^{eff} decreases marginally as solid volume increases. This is attributed to the fact that at very low liquid contents, the strength of the bond is mainly due to the cohesive strength between solid particles. Hence increase in solid volume increases the cohesive strength. For the case of a large liquid content, K_{break}^{eff} increases as solid volume increases. This is because, in the current case, the strength of the bond is mainly due to the liquid bridges and as solid volume increases, the liquid bridge strength decreases
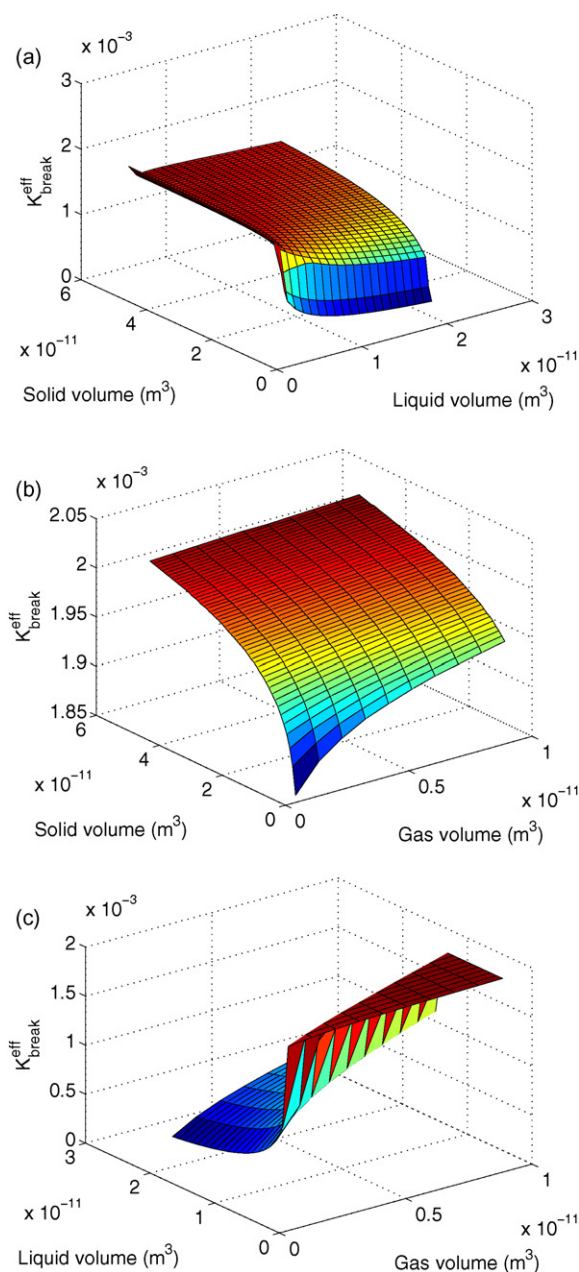
(due to a smaller liquid-to-solids ratio). The sharp peak seen in the figure as solid volume and liquid volume approach zero is due to negligible solid cohesive forces and liquid bridge forces that result in an exponential increase in K_{break}^{eff}. In Fig. 2 b, it can be seen that there is an increase in K_{break}^{eff} as both solid and gas volumes increase. This is due to the fact that at a constant liquid volume, increases in solid and gas volumes cause the liquid bridge strength to decrease significantly. In Fig. 2 c, it is observed that there is an increase in K_{break}^{eff} as liquid volume decreases and gas volume increases. This is because liquid directly affects the liquid bridge strength and gas volume adversely affects the liquid bridge strength.

The above mechanistic breakage kernel is then qualitatively compared with an existing empirical and semi-empirical breakage kernel from the literature. The empirical kernel is a power law expression based on experimental observations proposed by Pandya and Spielman (1983) and is

Table 2 – Parameter sensitivity with respect to material properties.

Time (s)	$\frac{\partial F}{\partial \gamma_s}$	$\frac{\partial F}{\partial \gamma_l}$	$\frac{\partial F}{\partial \mu_l}$	$\frac{\partial F}{\partial \phi}$	$\frac{\partial F}{\partial \rho_s}$	$\frac{\partial F}{\partial \rho_l}$	$\frac{\partial F}{\partial E_p}$	$\frac{\partial F}{\partial \sigma_p}$	$\frac{\partial F}{\partial e_p}$	$\frac{\partial F}{\partial circ}$	$\frac{\partial F}{\partial C_d}$	$\frac{\partial F}{\partial TSA}$
1	0	3.982	2.52	8.77	1.15	0.10	3.21	0.31	0.07	0	0	1.31
10	0	3.95	2.50	8.67	1.14	0.09	3.19	0.31	0.07	0	0	1.30
40	0	3.84	2.44	8.34	1.12	0.09	3.12	0.30	0.07	0	0	1.28
80	0	3.70	2.36	7.97	1.08	0.09	3.04	0.29	0.07	0	0	1.25
250	0	3.14	2.02	6.32	0.56	0.08	2.70	0.25	0.06	0	0	1.12
500	0	2.43	1.58	4.61	0.77	0.06	2.22	0.20	0.05	0	0	0.93
800	0	2.10	1.42	3.99	0.66	0.06	1.83	0.18	0.05	0	0	0.84
1000	0	2.27	1.57	4.17	0.74	0.06	2.08	0.20	0.07	0	0	0.95
1500	0	2.75	1.97	4.79	0.96	0.08	2.81	0.25	0.07	0	0	1.26
1800	0	3.06	2.22	5.27	1.11	0.09	3.30	0.28	0.09	0	0	1.45

defined by Eq. (55).

$$K_{break}^{empirical}(s, l, g) = P_1 G(R(s, l, g))^{P_2} \qquad (55)$$

where $K_{break}^{empirical}$ is the breakage kernel, P_1 and P_2 are adjustable constants, G is the shear rate in the system and R is the particle radius. The semi-empirical kernel used in the works of Selomuya et al. (2003) and Soos et al. (2006) is defined in Eq. (56) as

$$K_{break}^{semi-empirical}(s, l, g) = \left(\frac{4}{15\pi} \right)^{1/2} \times G \times \left(-\frac{B}{G^2 R(s, l, g)} \right) \qquad (56)$$

where B is an adjustable parameter. Values used for all adjustable constants and shear rates are taken from Table 2 in Soos et al. (2006). Fig. 3 a–c depicts the simulated shapes of the empirical breakage kernel with respect to two dimensions, keeping the third constant. It can be seen that there is no distinction between the three graphs and that there is a monotonic increase of the kernel metric in all three dimensions. This is incongruous to expected phenomenological behaviour. Firstly, although the increase in liquid content increases the volume of the particle, it also increases the liquid bridge strength. Secondly, increase in the solid volume would reduce the overall change in momentum upon collision (assuming total kinetic energy is constant), thereby resulting in a lesser impact force. Both these reasons negate a straightforward monotonic increase in the solid and liquid dimensions. Similarly, the shapes in Fig. 4, depict the shapes of the semi-empirical breakage kernel. It can be seen that the kernel metric is approximately constant in all three dimensions and spatial variations, effectively likening it to a constant kernel which is unable to account for the phenomenological behaviour of granule breakage. However, the above described empirical and semi-empirical kernels have been quantitatively validated (Soos et al., 2006) and in another study a constant breakage kernel was used to quantitatively describe breakage kinetics (Tan et al., 2004). This essentially shows that kernels that are fundamentally unsound, can still predict breakage kinetics, by tuning adjustable constant(s) that serve to compensate for any phenomenological mismatch. This approach is the spawn of a lack of a mechanistic understanding of the granule breakage mechanism. However, a mechanistic understanding/model of the breakage process is preferable due to advantages such as the predictive capabilities of the model. In the following sections the breakage kernel is further tested both qualitatively and quantitatively to ascertain its validity and use in the population balance framework.
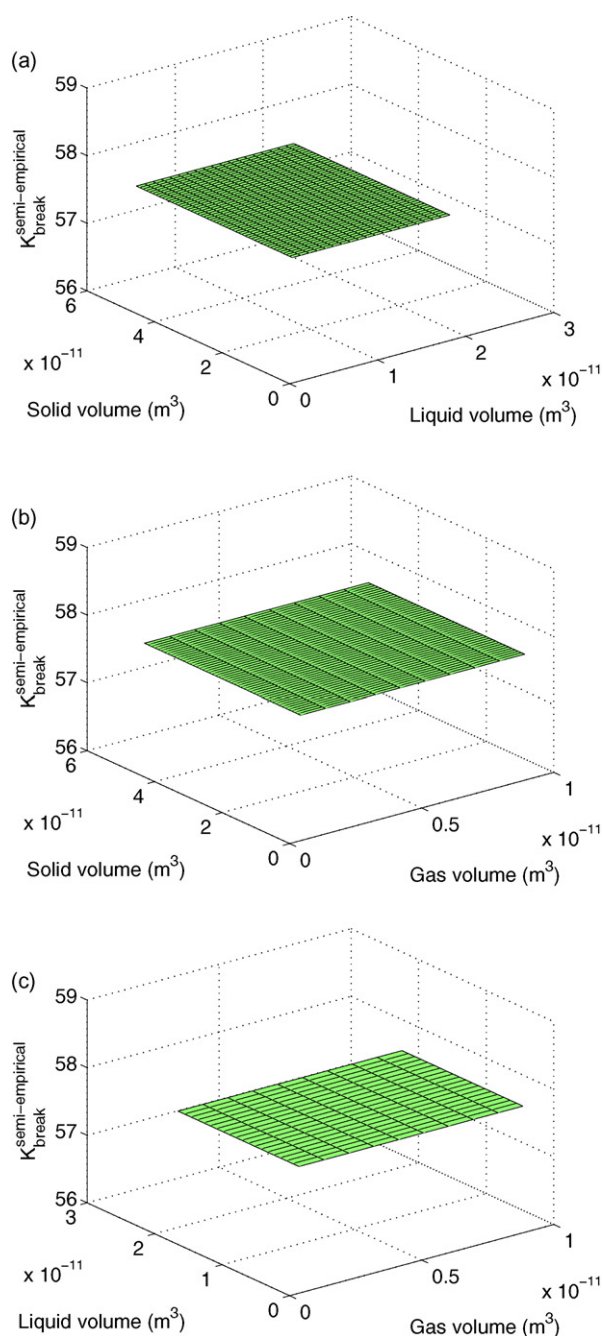
4.2. Test of breakage kinetics

Fig. 5 depicts the a semi-log plot of the fraction of particles remaining in the initial seed (i.e., $d_0 = 549\,\mu m$) as a function of
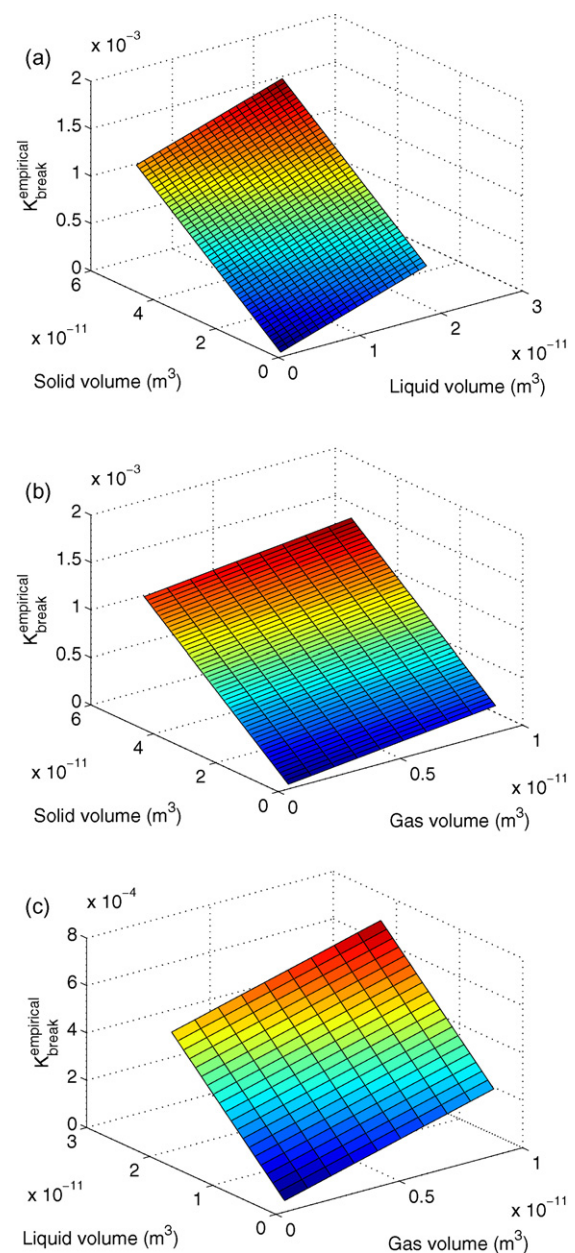
Fig. 3 – Shape of the empirical kernel (Eq. (55)) with respect to two dimensions keeping the third constant: (a) volume of gas constant, (b) volume of liquid constant and (c) volume of solid constant.

(a)

(b)

(c)

Fig. 4 – Shape of the semi-empirical kernel (Eq. (56)) with respect to two dimensions keeping the third constant: (a) volume of gas constant, (b) volume of liquid constant and (c) volume of solid constant.

time. First order breakage kinetics should yield a straight line with gradient $-K$. It is a good test of the form of the breakage model and is independent of the choice of breakage function. From Fig. 5, it can be seen that a straight line is produced with $-K = 6.42 \times 10^{-4}$ s^{-1}.

4.3. Decoupling the manner of granule breakage

In the experimental findings of Smith (2008), it was reported that the primary manner of granule breakage in high-shear mixers were due to particle–impeller collisions. This was followed by particle–wall collisions and particle–particle collisions. Possible reasons for this occurrence could be (1) higher probability of particles colliding with the impeller, (2) higher impact force generated by the impeller, followed by the walls,
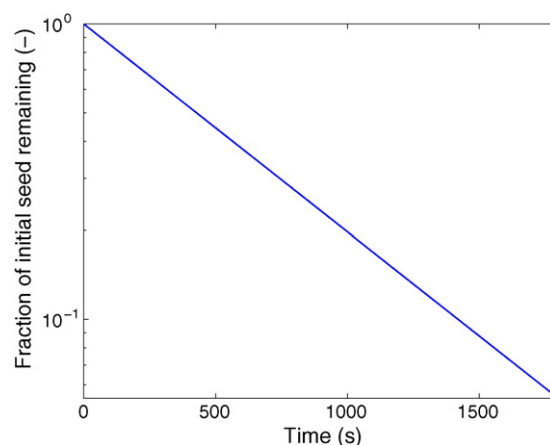
Fig. 5 – Plot of first order breakage kinetics.

(3) larger Young's modulus of the impeller result in less deformation resulting in a smaller contact area, hence higher external stress. Although Smith (2008) reported their finds for limited number of granulation recipes, they intimated that this would be a general trend for the case of high-shear granulation. However, undertaking numerous experiments altering material properties and process/design parameters to confirm their postulation would be exceedingly laborious and time-consuming. The ability to model and predict the experimentally observed trends *in-silico* would be very useful. Altering any parameters and properties in the model would also be convenient. Fig. 6 a and b depicts the evolutions of total particles and average diameter of each individual manner of granule breakage as well as their combined effect for a typical granule recipe and granulator geometry (see Table 1). In the current simulation, based on the surface areas, $P_p = 0.18$, $P_w = 0.55$, and $P_i = 0.27$, where P_p is the probability of a particle hitting any other particle, P_w is the probability of a particle hitting a wall surface and P_i is the probability of a particle hitting the impeller surface. Results show that the main manner of particle breakage is due to particle–impeller collisions followed by particle–wall collisions and then particle–particle collisions. The effects of fluid forces are negligible compared to the above collisions. It must be noted that the probabilities assigned for each collision can be subject to change depending on more exact knowledge of collisions. For instance, Smith (2008) reported that a large number of particles underwent collisions with the impeller in the impeller zone. Hence, a larger probability may be assigned to particle–impeller collisions. Either way, the breakage model is extremely useful in decoupling the manner of breakage based on the intrinsic material properties as well as user-defined process and design parameters. Model results are consistent with experimental findings and this lends credence to the validity of the model.

4.4. Evolutions/distributions of granule properties under nominal conditions

Fig. 7 a depicts the simulated temporal evolution of the total particles in the system which increases due to particle breakage. It can be seen that the rate of breakage decreases with time and this is attributed to the fact that as the average size of the granule decreases, the rates of breakage decrease as well. Fig. 7 b shows the decrease in average particle diameter with time and this is consistent with granule breakage behaviour. Fig. 7 c and d depicts the change in average porosity and
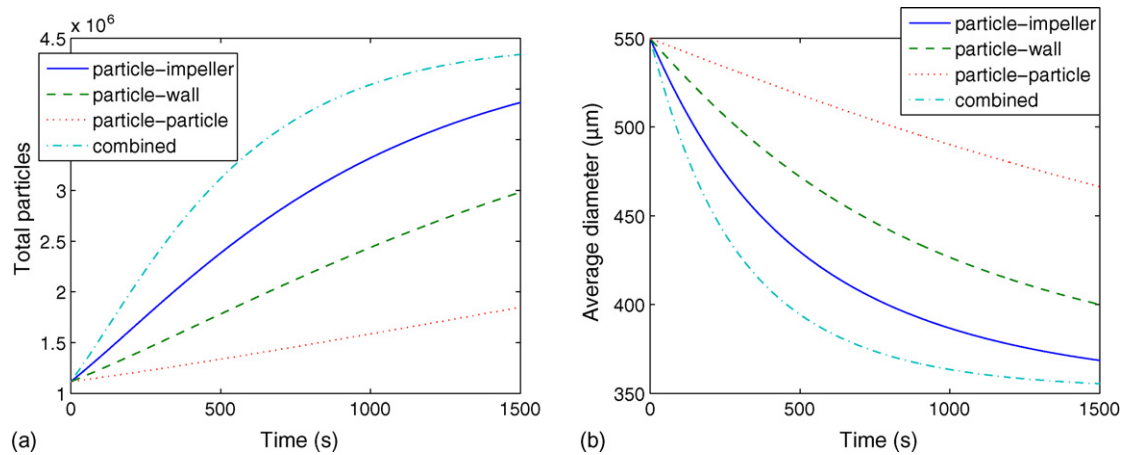
Fig. 6 – Evolution of (a) total particles and (b) average diameter, for the various manner of granule breakage.

binder content with time respectively. Average binder content reported remains constant throughout as no binder is added or removed to/from the system. A marginal increase is observed for average porosity and this attributed to the consolidation effect not strong enough as compared to particle breakage, to effect any decrease in particle porosity. Fig. 8 a–e depicts the end-point two-dimensional distribution of total particles with respect to particle diameter and fractional binder content. As seen in the plots, the particles in the initial seed undergo breakage to form a smaller mode of particles with a larger distribution width. This observation is consistent with experimental trends.

4.5. Dynamic sensitivity analysis of model inputs

In this section, a dynamic parameter-driven sensitivity analysis of the model output (particle density distribution, F) is performed. A detailed sensitivity analysis has two main purposes. Firstly, the importance of a model input is ascertained by quantifying its effect on the output. The model inputs can be ranked in order of importance. More effort and resources can be spent on sensitive inputs, and insensitive inputs can be kept constant during the model calculations. This has the potential of reducing the overall dimensional space of the problem. Alternatively, the process can be
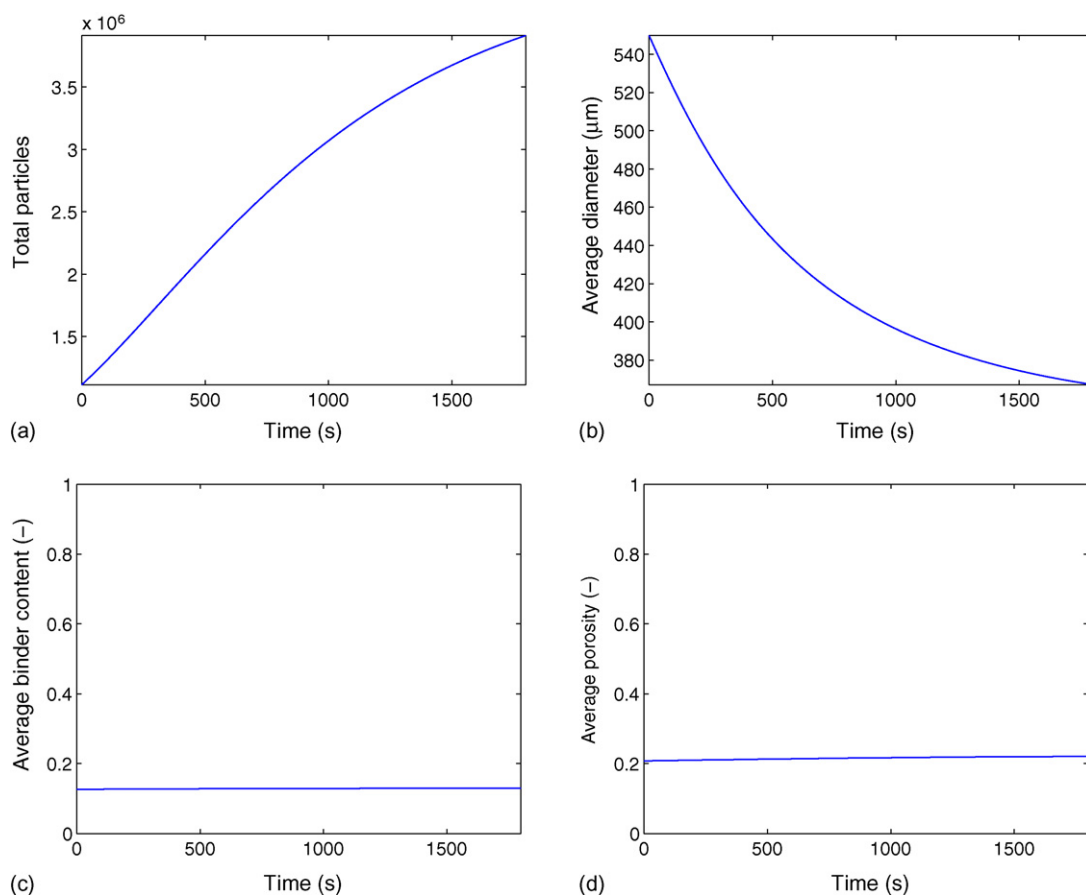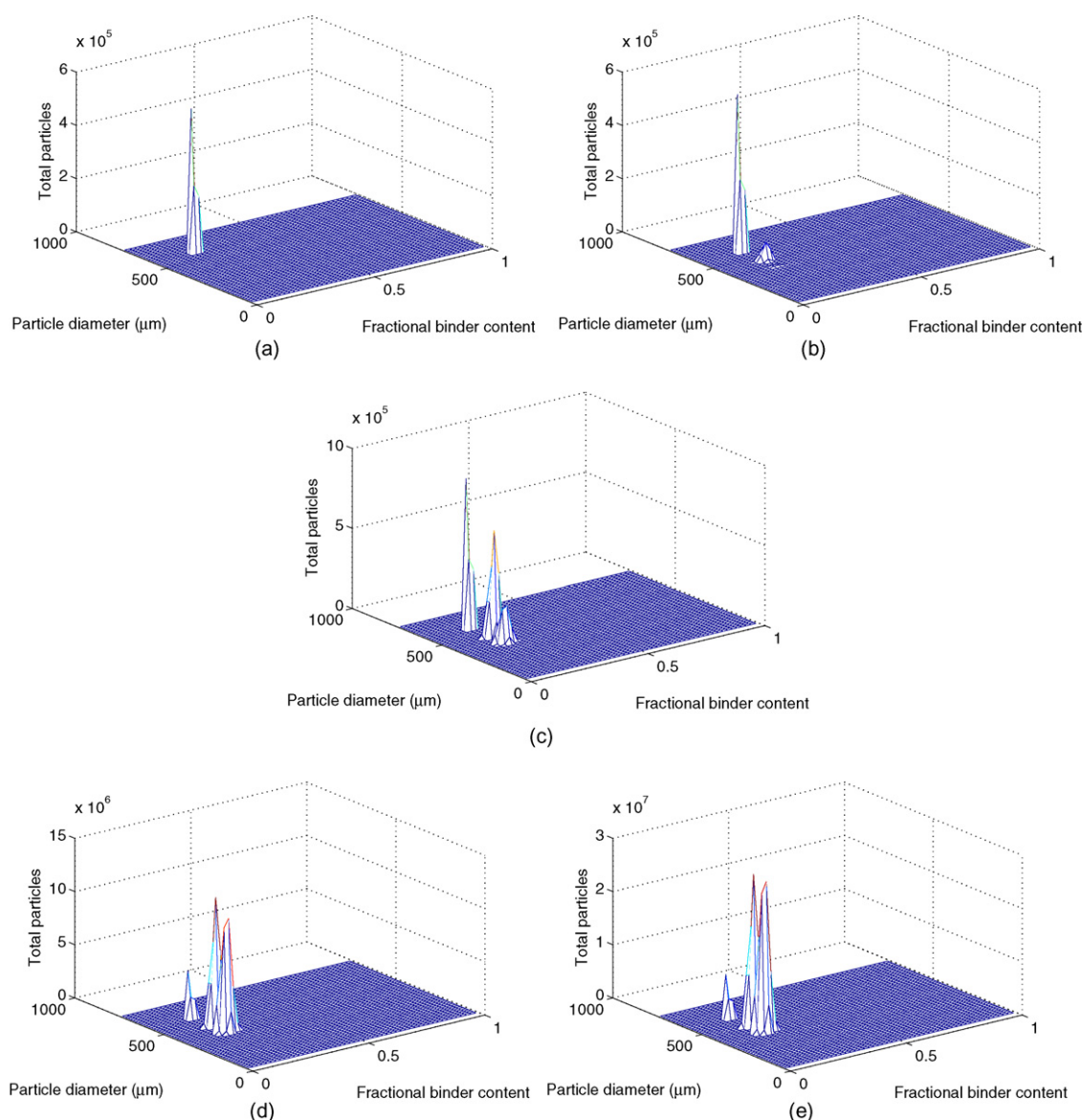

Fig. 7 – Evolution of (a) total particles, (b) average diameter, (c) average binder content and (d) average porosity.

Fig. 8 – Evolution of the granule size distributions under breakage at various time instances: (a) $t = 0$ s, (b) $t = 50$ s (c) $t = 200$ s, (d) $t = 500$ s and (e) $t = 1790$ s.

redesigned to increase the input sensitivities. This serves to potentially increase the overall controllability of the process. Secondly, there are always uncertainties involved in any of the experimentally measured model inputs (e.g. viscosity, surface tension, contact angle, etc.). As a result, these uncertainties may propagate through the model to the output and can yield erroneous results. A sensitivity analysis would identify important inputs for which accurate measurements are required. For less sensitive inputs whose uncertainties do not affect the model output, a high degree of accuracy in the measurements may not be required.

The sensitivity coefficient used in this work is defined to be the first order partial derivative of the model output (F) with respect to the model inputs at the particular times when potential measurements are available (see Eq. (57)) . In the current scenario, 10 measurements at intermittent sampling times from 1 s to 1800 s are considered.

$$\text{sensitivity coefficient} = \frac{\partial F(s, l, g)}{\partial \theta_p}\Big|_{t_n} \qquad (57)$$

Here, θ_p represents the spectrum of model inputs and t_n depicts the sampling times. A second order centered difference formula for the first derivative is utilised. Since the model is nonlinear and perhaps non-monotonic, a $\pm 50\%$ is applied to the inputs. To effectively compare sensitivity coefficients, a scaling factor was introduced to scale the sensitivity coefficients (Kou et al., 2005)(see Eq. (58)):

$$\text{sensitivity coefficient} = \frac{\hat{\theta}_p}{\hat{F}(s, l, g)|_{t_n}} \frac{\partial F(s, l, g)}{\partial \theta_p}\Big|_{t_n} \qquad (58)$$

Here, $\hat{\theta}_p$ is the current value of the model input prior to making a change and $\hat{F}(s, l, g)$ is the current value of the model output at time t_n, prior to making any change. Tables 2 and 3 depict the respective sensitivity coefficients of the particle density with respect to material properties and process/design parameters.

Results show that the most sensitive parameter is the volume fraction of the daughter particles $\theta_{v_{a,b}}$. This is expected because as $\theta_{v_{a,b}}$ varies, the daughter particles occupy different finite volumes (bins) which can have very different breakage

Table 3 – Parameter sensitivity with respect to process and design properties.												
Time (s)	$\frac{\partial F}{\partial \mu_a}$	$\frac{\partial F}{\partial E_w}$	$\frac{\partial F}{\partial E_i}$	$\frac{\partial F}{\partial \sigma_w}$	$\frac{\partial F}{\partial \sigma_i}$	$\frac{\partial F}{\partial e_w}$	$\frac{\partial F}{\partial e_i}$	$\frac{\partial F}{\partial \theta_{v_a}}$	$\frac{\partial F}{\partial WA}$	$\frac{\partial F}{\partial IA}$	$\frac{\partial F}{\partial A}$	$\frac{\partial F}{\partial \frac{da}{dt}}$
1	0	0.64	1.12	0.03	0.21	0.28	0.44	479.76	0.97	2.49	0	0
10	0	0.63	1.11	0.04	0.20	0.27	0.44	66.38	0.96	2.47	0	0
40	0	0.62	1.09	0.03	0.20	0.27	0.43	21.56	0.95	2.43	0	0
80	0	0.60	1.07	0.03	0.20	0.28	0.41	13.89	0.93	2.36	0	0
250	0	0.52	0.94	0.03	0.17	0.22	0.36	8.65	0.85	2.09	0	0
500	0	0.42	0.77	0.02	0.14	0.17	0.29	7.42	0.73	1.73	0	0
800	0	0.38	0.63	0.02	0.12	0.16	0.25	7.03	0.61	1.39	0	0
1000	0	0.42	0.71	0.02	0.13	0.18	0.28	7.18	0.71	1.57	0	0
1500	0	0.54	0.93	0.03	0.16	0.23	0.35	7.37	0.98	2.10	0	0
1800	0	0.62	1.08	0.03	0.19	0.26	0.39	7.43	1.16	2.44	0	0

Only θ_{v_a} is listed as a model input as it is implicit that $\theta_{v_b} = 1 - \theta_{v_a}$.

kernel metrics ($k^{\text{eff}}_{\text{break}}$). As a result, the breakage rates are significantly different for even marginal changes in $\theta_{v_{a,b}}$. Results also show that changes in model inputs such as drag coefficient (C_d), circularity index (circ), viscosity of air (μ_a), solid surface tension (γ_s) and the proportionality constant (A) do not influence the model output. C_d and μ_a influence the fluid forces which are negligible compared to the more dominant particle–particle, particle–wall and particle–impeller forces and as a result have no effect on the output. Similarly, circ and γ_s affect the frictional forces of the liquid bridges which are negligible compared to the more dominant capillary and viscous forces. The fact that a change in A does not influence the model output bodes well with the current mechanistic breakage model, as large changes in A would be required to effect any change in model output. This coupled with the sensitivity coefficients for other model inputs show that the model is primarily driven by fundamental material properties and process/design parameters rather than any empirical constant. It can also be observed that in terms of uncertainty propagation, more accurate measurements would be required for model inputs such as the Young's modulus of the impeller (E_i) and wall (E_w), binder surface tension (γ_l), binder viscosity (μ_l) and contact angle (ϕ).

5. Model validation studies in high shear granulation

Model validation is an important step in the overall development and formulation of a model. A model that has been successfully validated can be used for further process analysis, to facilitate design, optimisation, control and scale-up of the process. In the case of granulation, validation of a first-principles based granule breakage model has not been reported in the literature. The only study by Dhanarajan and Bandyopadhyay (2007) showed some initial work towards model validation. However, their study was restricted to the one-dimensional validation of evolutions of granule weight fractions (for small, large and intermediate granules) and did not account for distributions in granule size and/or evolutions of binder content and porosity. Furthermore, their model was validated for only one experimental setting without examining its potential to predict granule output (e.g. the weight fractions) at different experimental settings. It must be noted that the ability of the model to accurately predict specific output (e.g. evolutions and distributions) is a key component that distinguishes sound first-principles based models from empirical or semi-empirical models. The latter by virtue of

their lack of a physical basis, are not viable for prediction purposes. Therefore, in this study, the developed breakage model is validated at a nominal set of experimental conditions and the tuned model is used to predict with greater accuracy multi-dimensional evolutions of distributions at other operating conditions and/or formulations.

5.1. Materials and methods

For the high-shear granulation experiments, glass-ballotini (Potters, UK) was used as the primary powder. This material had a volume mean diameter (d_{30}) of 112 μm and a size range of 75 μm to 150 μm. The measured skeletal density of the material was 2480 kg m^{-3}. Polyvinyl alcohol (Elvanol T66, Du Pont, USA) in water (PVOH-H$_2$O) (2.5% and 5% concentration by mass) was used as the liquid binder. Degree of hydrolysis and molecular weight of PVOH were 99 mol% and 50000 respectively.

The high-shear granulation experiments were performed using a laboratory scale food processor mixer (Kenwood). The high-shear mixer is a vertical axis granulator with a diameter of 0.2 m and a height of 0.15 m. All the experiments were conducted with an impeller angular speed of 500 rpm. For each experiment, approximately 500 g of dry powder was granulated with PVOH-H$_2$O (2.5%) to form larger wet granules. These granules were then sieved and granules within the 500–600 μm size range were then used as the starting material to perform the breakage-only granulation experiments. Due to only limited amount of residual binder and no additional input of binder, granule breakage is dominant over granule growth. Samples were taken at distinct intervals by scooping approximately 40 g of material from different locations within the mixer. In order to test the reproducibility of the sampling method, one experiment was performed where the granulation process was ceased after 10 min and four samples were withdrawn from the mixer. By comparing the standard deviation across the samples, it was realised that there was minimal sampling error. The samples were subsequently dried overnight at ambient temperature. After drying, the granule size distribution (GSD) was determined via a particle size and shape analyser (Ankersmidt). An average binder content at different sampling times was measured prior to the overnight drying, by means of thermo-gravimetry. In a similar fashion, the average porosity was determined by means of pycnometry, after the overnight drying. All experiments and measurements were performed thrice to ensure reproducibility.

5.2. *Results and discussion*

The proposed experimental design serves to emphasize granule breakage such that aggregation rates can be neglected. Nucleation does not apply as it is restricted to nuclei formed from primary particles and in the current predominantly breakage-only case, the initial feed are larger granules. Therefore, the population balance model accounting for only breakage and consolidation is validated by comparing the simulated output with experimental measured data. Granule samples were taken out from the drum granulator at time instances of 60 s, 120 s, 240 s and 600 s. In the model, the primary particles are mono-dispersed with an average diameter of 550 μm. Other model inputs such as the initial number of seed particles and those listed in Table 1(with the exception of ϕ) were set as per experimental conditions (e.g. D_{lower} = 150 μm as this corresponds to the lower limit of the primary particle diameter and once the particles reach this diameter, they cannot break into smaller constituent particles). A and ϕ (for which accurate measurements were not available) and the consolidation constant (c) were used as tuning parameters for matching the predicted model outputs with experimental measurements of the granule attributes. The first set of data (case 1) was used to tune the model i.e., estimate the three parameters in the model. Subsequently, the tuned model was used to predict the GSD and evolution of average diameter at different operating conditions/formulations (cases 2 and 3). Case 1 corresponds to a binder viscosity of 0.0052 Pa s (2.5% PVOH-H$_2$O) and binder-to-solids ratio of 0.125 (i.e., (L/S) = 0.125) . Case 2 corresponds to a binder viscosity of 0.022 Pa s (5.0% PVOH-H$_2$O) with (L/S) = 0.125. Case 3

corresponds to a binder viscosity of 0.0052 Pa s with (L/S) = 0.15. All other material properties and process/design parameters were the same for the three cases. The model was tuned by systematically varying the adjustable constants (i.e., c, A and ϕ) in the simulation mode, to provide an acceptable match via visual inspection between the model output and the experimentally measured data. Using the first set of data, the parameters, $c = 5 \times 10^{-5}$, $A = 1.5 \times 10^{-9}$ and $\phi = 0.694$ were obtained. Simulations were performed to identify the lower and upper bounds of the adjustable parameters to ensure that the assumed values correspond to within the range of experimentally observed breakage behaviour. Based on the results, the bounds were identified to be $0 \leq c \leq 0.5$, $1 \times 10^{-10} \leq A \leq 1 \times 10^{-7}$ and $0.5 \leq \phi \leq 0.9$ and it can be seen that the adjustable constants reported lie within these ranges. These values for the parameters were used thereafter for the second and third set of data. For instance, if the rotational speed of the mixer is changed, the tuning parameters would remain the same, but u_0 (model parameter in the breakage kernel, indicating rotational speed) will be updated to the new value. This applies to other material and process variables. In this manner, the breakage kernel (upon successful prediction of granule dynamics at other operating conditions) can be utilised as a predictive model which would be useful for design, scale-up and control.

Fig. 9 a depicts the simulated temporal evolution of the total particles in the system which increases due to particle breakage, for cases 1–3. Due to the higher binder viscosity in case 2, the liquid bridge strength is higher which in turn slows down the rate of breakage compared to case 1. Similarly, due to a higher binder content in case 3 as compared to case 1, the liq-
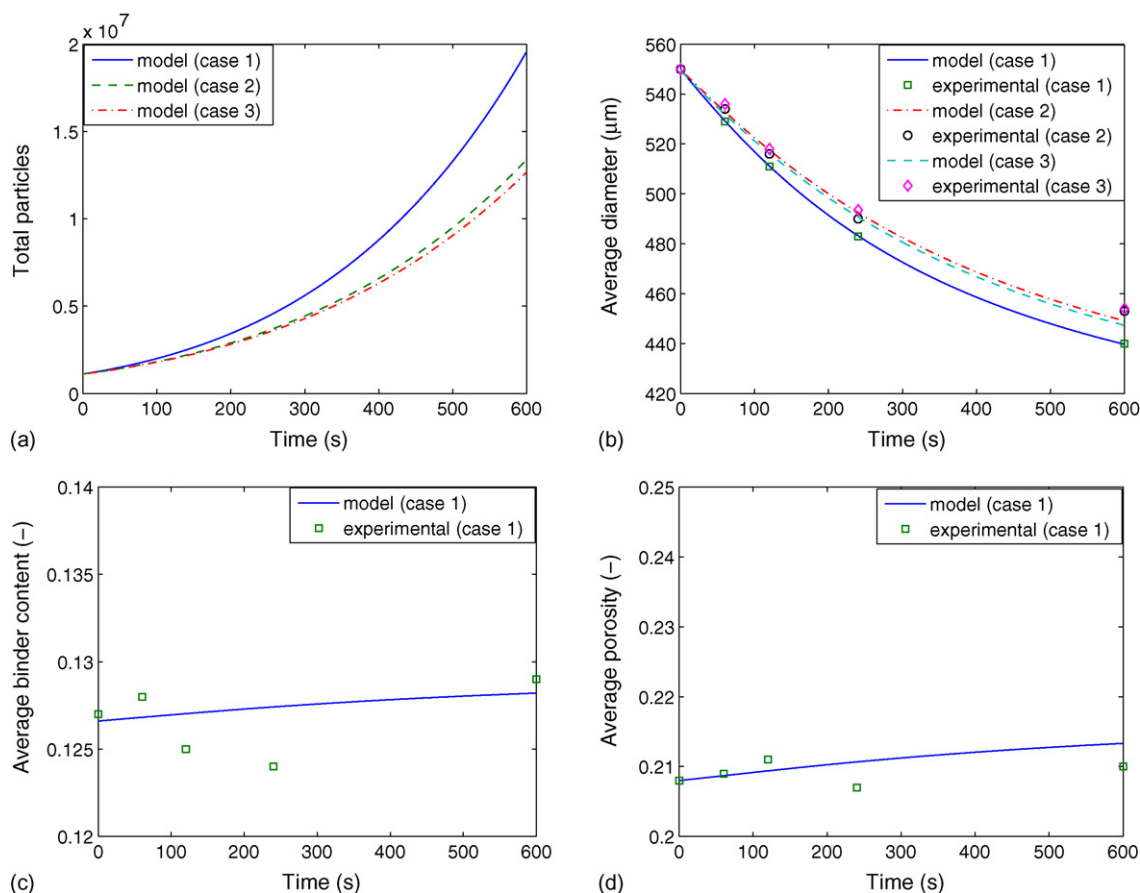

Fig. 9 – Comparisons between temporal evolutions of experimentally measured and model predictions of (a) total particles, (b) average diameter, (c) average binder content and (d) average porosity.
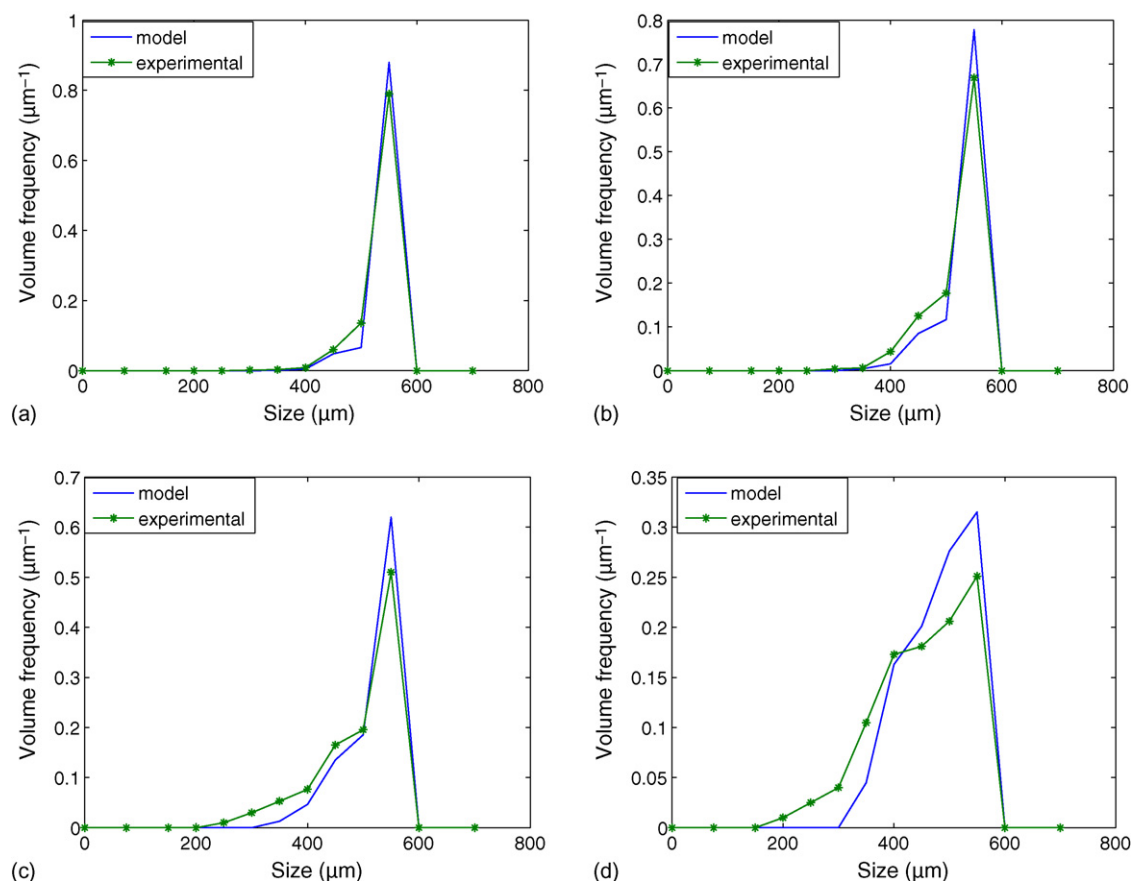
Fig. 10 – Comparisons between simulated and experimental GSDs for case 1 for (a) $t = 1$ min, (b) $t = 2$ min, (c) $t = 4$ min and (d) $t = 10$ min.
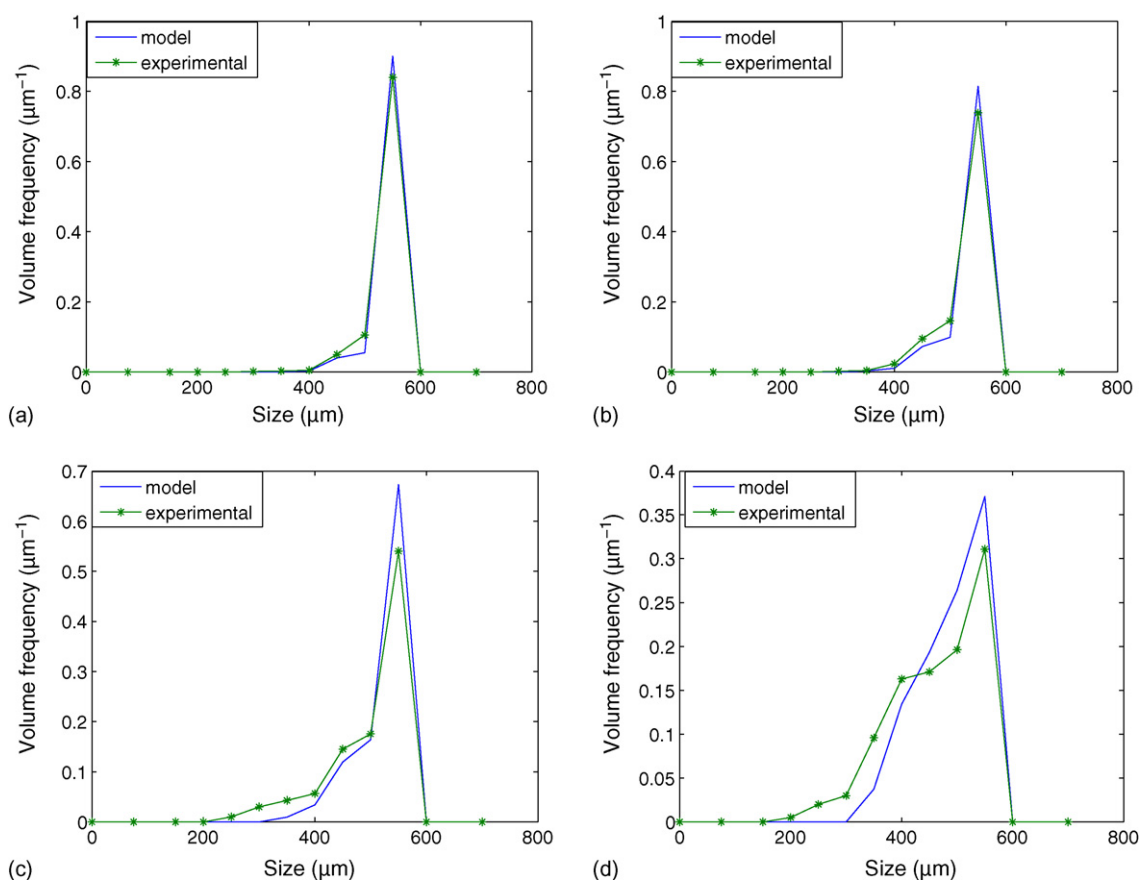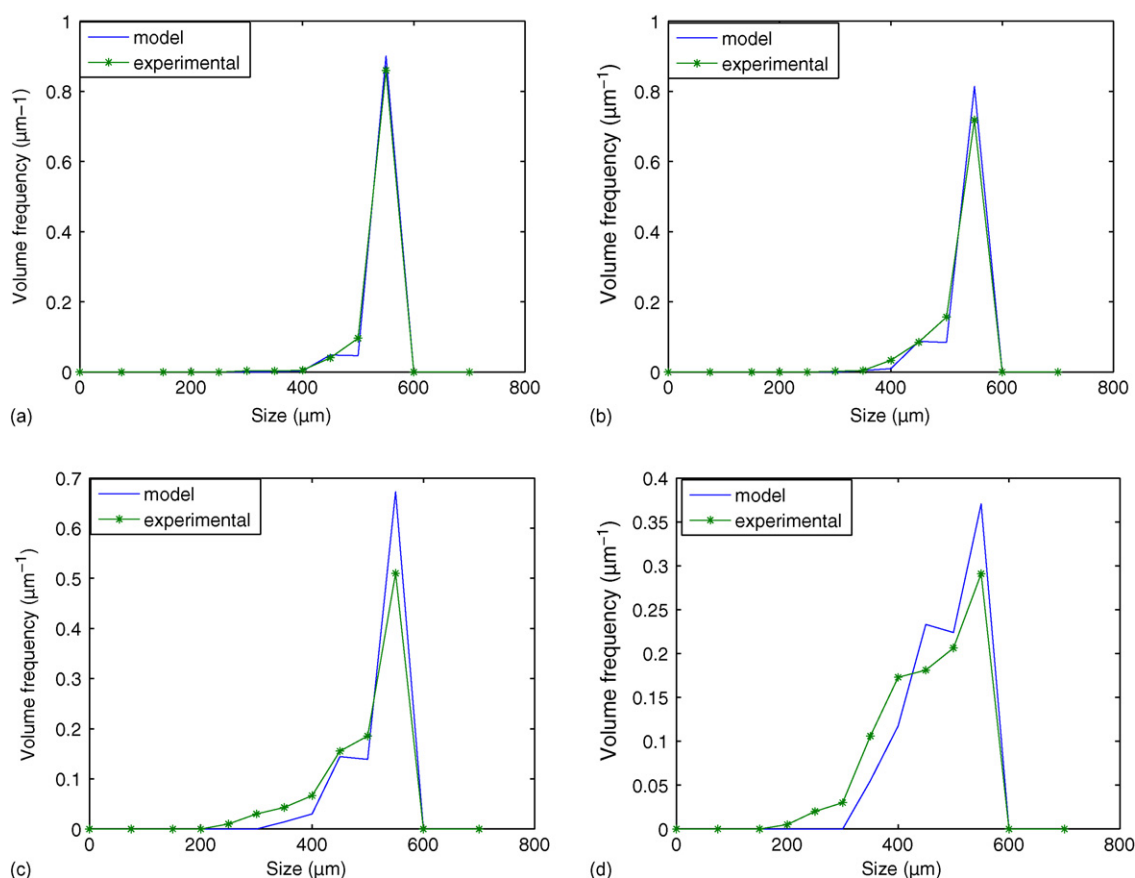

Fig. 11 – Comparisons between simulated and experimental GSDs for case 2 for (a) $t = 1$ min, (b) $t = 2$ min, (c) $t = 4$ min and (d) $t = 10$ min.

Fig. 12 – Comparisons between simulated and experimental GSDs for case 3 for (a) t = 1 min, (b) t = 2 min, (c) t = 4 min and (d) t = 10 min.

uid bridge strength is higher resulting in reduced breakage. Fig. 9 b shows the change in average particle diameter with time. The model is able to capture the particle level phenomena and sensitivities of the process resulting in a close match between the simulated profile and experimentally measured data for all cases. Due to the higher liquid bridge strength, average particle diameter for cases 2 and 3 is higher than that of case 1. Fig. 9 c and d depicts the change in average binder content and porosity with time respectively, for case 1. It can be seen that within acceptable measurement error, the model is able to capture of the range of these average properties. Average binder content reported remains constant throughout as no binder is added or removed to/from the system. A marginal increase is observed for average porosity and this attributed to the consolidation effect not strong enough as compared to particle breakage, to effect any decrease in particle porosity. Similar observations were obtained for cases 2 and 3.

Figs. 10 a–d, 11 a–d and 12 a–d show the model and experimental GSDs at each time instance corresponding to the intermittent sampling times (i.e., 60 s, 120 s, 240 s and 600 s) during the experiment for cases 1, 2 and 3 respectively. The GSDs are represented as the normalised volume frequency (V_f) of granules with respect to granule diameter (D) as defined in Eq. (59):

$$V_f(D, t) = \frac{F(D, t)}{\int F(D, t) dD} \times \frac{V(D)}{\int V(D) dD} \qquad (59)$$

where V is the particle volume. A clear progression is observed during the course of granulation whereby particles undergo breakage forming smaller sized particles, which is depicted by

a gradual reduction in the peak corresponding to 550 μm. It can be seen that the tuned model is able to accurately capture the experimental GSD for case 1 and thereafter able to accurately match/predict accurately the GSD for cases 2 and 3.

6. Conclusions

In this chapter, the theoretical development of a novel breakage kernel was presented. The kernel was based on the underlying physics and chemistry of the granule breakage phenomenon. The kernel was formulated as a quotient of external stress applied over the intrinsic strength of a granule, which is analogous to the Stokes' deformation criteria and is a realistic characterisation of granule breakage. The external stress is modelled taking into account particle–particle, particle–wall and particle–impeller collisions; and the contact area formed upon impact. The intrinsic strength is characterised by the liquid bridge forces which are determined mainly by the capillary forces, viscous forces and frictional forces. The derived kernel is a function of several important material properties (i.e., powder and liquid binder properties) and process/design parameters, which influence the granule intermittent and end-point properties. The kernel shapes from the mechanistic model are able to qualitatively predict the expected breakage behaviour. When compared with an empirical and semi-empirical kernel, it could be seen that the mechanistic kernel could account for the rate differences in accordance with expected phenomenological behaviour of granule breakage, unlike the empirical and semi-empirical kernels. A simulation study was undertaken to test the form of the breakage model and results showed that the model

accurately described the breakage kinetics. The effects of the key material properties and process/design parameters on the granule output were studied and qualitatively confirmed that the kernel/model predictions were accurate. A dynamic sensitivity analysis of the model inputs were performed and results showed that the granule output (particle density distribution) was sensitive to variations in expected properties/parameters such as contact angle, viscosity, surface tension and volume fraction of daughter particles formed. This along with the fact that the influence of the empirical constant in the kernel does not dominate the mechanistic parameters, corroborates the overall effectiveness of the kernel development. Successful experiments were also performed to mimic predominantly breakage only behaviour whereby the rate of breakage was greater than that of growth enhancing mechanisms such as nucleation and aggregation. Quantitative validation of the GSDs between the model predictions and those obtained from experiments for the various cases showed very good agreement. The model predictions for the average properties (i.e., size, binder content and porosity) were in close agreement to the experimentally measured data. Overall, these results are promising toward a comprehensive first-principles predictive model for the granulation process, that can help reduce the number of labour and capital intensive experiments required for a more in-depth understanding of the granulation process.

Acknowledgements

References

Bardin, M., Knight, P.C. and Seville, J.P.K., 2004, On control of particle size distribution in granulation using high shear mixers. Powder Technology, 140: 169–175.

Biggs, C.A., Sanders, C., Scott, A.C., Willemse, A.W., Hoffman, A.C., Instone, T., Salman, A.D. and Hounslow, M.J., 2003, Coupling granule properties and granulation rates in high shear granulation. Powder Technology, 130: 162–168.

Dhanarajan, A.P. and Bandyopadhyay, R., 2007, An energy-based population-balance approach to model granule growth in high-shear wet granulation processes. AIChE Journal, 43: 927–934.

Hotta, K., Takeda, K. and Iinoya, K., 1974, The capillary binding force of a liquid bridge. Powder Technology, 10: 231–242.

Immanuel, C.D. and Doyle, F.J., III., 2005, Solution technique for a multi-dimensional population balance model describing granulation processes. Powder Technology, 156: 213–225.

Iveson, S.M., 2002, Limitations of one-dimensional population balance models of wet granulation processes. Powder Technology, 124: 219–229.

Iveson, S.M., Litster, J.D., Hapgood, K.P. and Ennis, B.J., 2001, Nucleation, growth and breakage phenomena in agitated wet granulation processes: a review. Powder Technology, 117: 3–39.

Knight, P.C., Instone, T., Pearson, J.M.K. and Hounslow, M.J., 1998, An investigation into the kinetics of liquid distribution and growth in high shear mixer agglomeration. Powder Technology, 97: 246–257.

Kou, B., McAuley, K.B., Hsu, C.C., Bacon, D.W. and Yao, K.Z., 2005, Mathematical model and parameter estimation for gas-phase ethylene homopolymerization with supported metallocene catalyst. Industrial Engineering Chemistry Research, 44: 2428–2442.

Lian, G., Thornton, C. and Adams, M.J., 1993, A theoretical study of the liquid bridge forces between two rigid spherical bodies. Journal of Colloid Interface Science, 161: 138–147.

Litster, J.D., 2003, Scaleup of wet granulation processes: science not art. Powder Technology, 130: 35–40.

Litster, J.D. and Ennis, B.J., (2004). *The Science and Engineering of Granulation Processes*. (Kluwer Academic Publishers).

Liu, L.X., Smith, R. and Litster, J.D., 2008, Wet granule breakage in a breakage only high-shear mixer: effect of formulation properties on breakage behaviour, Powder Technology, 189: 158–164.

Luding, S., Clement, E., Blumen, A., Rajchenbach, J. and Duran, J., 1994, Anomalous energy dissipation in molecular-dynamics simulations of grains: the "detachment" effect. Physical Review E, 50: 4113–4124.

Mort, P.R., 2005, Scaleup of binder agglomeration processes. Powder Technology, 150: 86–103.

Pandya, J.D. and Spielman, L.A., 1983, Floc breakage in agitated suspensions: effect of agitation rate. Chemical Engineering Science, 38: 1983–1992.

Pinto, M.A., 2008, Modelling and control of biological systems, Ph.D. Thesis, Imperial College London.

Pinto, M.A., Immanuel, C.D. and Doyle, F.J., III., 2007, A feasible solution technique for higher-dimensional population balance models. Computers and Chemical Engineering, 31: 1242–1256.

Pinto, M.A., Immanuel, C.D. and Doyle, F.J., III., 2008, A two-level discretisation algorithm for the efficient solution of higher-dimensional population balance models. Chemical Engineering Science, 63: 1304–1314.

Poon, J.M.H., Immanuel, C.D., Doyle, F.J. and Litster, J.D., III., 2008, A three-dimensional population balance model of granulation with a mechanistic representation of the nucleation and aggregation phenomena. Chemical Engineering Science, 63: 1315–1329.

Poon, J.M.H., Ramachandran, R., Sanders, C.F.W., Glaser, T., Immanuel, C.D., Doyle III, F.J., Litster, J.D., Stepanek, F., Wang, F.Y. and Cameron, I.T., in press, Experimental validation studies on a multi-scale and multi-dimensional population balance model of batch granulation, Chemical Engineering Science.

Princen, H.M., 1968, The effects of capillary liquid on the force of adhesion between spherical particles. Journal of Colloid Interface Science, 26: 247–253.

Ramachandran, R., 2008, Multi-scale population balance modelling and controllability of granulation processes, Ph.D. Thesis, Imperial College London.

Reynolds, G.K., Fu, J.S., Cheong, Y.S., Hounslow, M.J. and Salman, A.D., 2005, Breakage in granulation: a review. Chemical Engineering Science, 60: 3969–3992.

Salman, A.D., Fu, J., Gorham, D.A. and Hounslow, M.J., 2003, Impact breakage of fertiliser granules. Powder Technology, 130: 359–366.

Sanders, C.F.W., Willemse, A.W., Salman, A.D. and Hounslow, M.J., 2003, Development of a predictive high-shear granulation model. Powder Technology, 138

Selomuya, C., Bushell, G., Amal, R. and Waite, T.D., 2003, Understanding the role of restructuring in flocculation: the application of a population balance model. Chemical Engineering Science, 58: 327–338.

Simons, S.J.R., (2007). *Granulation Handbook of Powder Technology* (11th edition). (Elsevier), pp. 1256–1351

Simons, S.J.R., Seville, J.P.K. and Adams, M.J., 1994, An analysis of the rupture energy of pendular liquid bridges. Chemical Engineering Science, 49: 2331–2339.

Smith, R., 2008, Wet granule breakage in high shear mixer granulators, Ph.D. Thesis, University of Queensland.

Soos, M., Sefcik, J. and Morbidelli, M., 2006, Investigation of aggregation, breakage and restructuring kinetics of colloidal dispersions in turbulent flows by population balance modeling and light scattering. Chemical Engineering Science, 61: 2349–2363.

Stachowiak, G.W. and Batchelor, A.W., (2005). *Engineering Tribology*. (Cambridge University Press).

Tan, H.S., Salman, A.D. and Hounslow, M.J., 2004, Kinetics of fluidised bed melt granulation. IV. Selecting the breakage model. Powder Technology, 143–144: 65–83.

Tan, H.S., Salman, A.D. and Hounslow, M.J., 2005, Kinetics of fluidised bed granulation. V. Simultaneous modelling of aggregation and breakage. Chemical Engineering Science, 60: 3847–3866.

Van den Dries, K., de Vegt, O.M., Girard, V. and Vromans, H., 2003, Granule breakage phenomena in a high shear mixer; influence of process and formulation variables and consequences on granule homogeneity. Powder Technology, 133: 228–236.

Verkoeijen, D., Pouw, G.A., Meesters, G.M.H. and Scarlett, B., 2002, Population balances for particulate processes—a volume approach. Chemical Engineering Science, 57: 2287–2303.

Willett, C.D., Johnson, S.A., Adams, M.J. and Seville, J.P.K., (2007). *Granulation Handbook of Powder Technology* (11th edition). (Elsevier), pp. 1316–1351